



Nickel-cobalt phosphate/graphene foam as enhanced electrode for hybrid supercapacitor

Abdulmajid Abdallah Mirghni^a, Kabir O. Oyedotun^a, Badr Ahmed Mahmoud^a,
Abdulahakeem Bello^{a,b}, Sekhar C. Ray^{c,d}, Ncholu Manyala^{a,*}

^a Department of Physics, Institute of Applied Materials, SARCHI Chair in Carbon Technology and Materials, University of Pretoria, Pretoria, 0028, South Africa

^b Department of Materials Science and Engineering, African University of Science and Technology, Abuja, Nigeria

^c Department of Physics, College of Science, Engineering and Technology, University of South Africa, Private Bag X6, Florida, 1710, South Africa

^d Science Campus, Christiaan de Wet and Pioneer Avenue, Florida Park, Johannesburg, 1710, South Africa

ARTICLE INFO

Keywords:

Nickel phosphate
Cobalt phosphate
Graphene
Energy storage
Supercapacitor
Hybrid device

ABSTRACT

Nickel-cobalt phosphate/graphene foam (40 mg) ($\text{NiCo}(\text{PO}_4)_3/\text{GF}$) composite was synthesized via a hydrothermal process and used as electrode material for supercapacitors. This work was done based on the fact that the electrochemical behavior of cobalt phosphate is similar to EDLC, while nickel phosphate is purely faradaic. Interestingly, the advantages of these two different mechanisms reflected on the results of $\text{NiCo}(\text{PO}_4)_3/\text{GF}$ as an electrode for supercapacitor. The crystal structure, morphology and texture of the synthesized materials were studied with XRD, Raman spectrum, SEM and BET. The electrochemical performance of the produced sample was investigated by cyclic voltammetry (CV), galvanostatic charge-discharge (GCD), and electrochemical impedance spectroscopy (EIS) in 1 M KOH electrolyte. $\text{NiCo}(\text{PO}_4)_3/\text{GF}$ 40 mg composite exhibited significantly improved specific capacity (86.4 mAh g^{-1}) much higher than pristine $\text{NiCo}(\text{PO}_4)_3$ (64 mAh g^{-1}) at 1 A g^{-1} due to the synergistic effect between the conductive GF and $\text{NiCo}(\text{PO}_4)_3$. Furthermore, the hybrid supercapacitor device ($\text{NiCo}(\text{PO}_4)_3//\text{AC}$) fabricated achieved the highest energy density of 34.8 Wh kg^{-1} and a power density of 377 W kg^{-1} at a specific current of 0.5 A g^{-1} . The hybrid device also showed 95% of capacity retention after 10000 charge-discharge cycles at a specific current of 8 A g^{-1} and 90% efficiency at floating time over 110 h at 5 A g^{-1} . These results make this composite to be a good candidate for electrochemical capacitors applications.

1. Introduction

Green energy difficulties are turn to be progressively basic in current world [1,2]. Recently, the growth of new and alternative energy storage devices with high-capability has become an area of interest for researchers [3–5]. Being unique energy storage devices, the energy densities of supercapacitors (SCs) are in-between that of batteries and the conventional capacitors, displaying a better values in terms of specific capacity and specific energy when compared to the conventional capacitors [6]. On the other hand, SCs offer superior power delivery i.e. quicker charge/discharge process leading to wider power density, better cyclability and comparatively less energy density than batteries [7,8]. Due to the new generations of electric and hybrid cars, SCs have attracted enormous consideration as an alternative to/or in complimentary capacity to batteries, thus, it is necessary to put in more efforts to improve the energy density of SCs. The key strategy to this, are the use

of pseudocapacitive materials and electrolytes having higher potential (ionic liquids, lithium salts and organic electrolytes) and also designing diverse and efficient dimensionalities of materials [9–11]. Recent studies have shown that combining battery-like and double layer materials can expand the capacitance and cell potential of SCs [12].

SCs can either be pseudocapacitors (PCs) or electrochemical double-layer capacitors (EDLCs). PCs are based on oxide materials and conductive polymers due to the fact that they have high electrochemical activities (electrochemical redox reactions) which leads to very high capacitance values, while in EDLC, there is charge separation at the electrode/electrolyte interfaces that are responsible for the capacitance [13,14]. The energy density of SC is commonly dependent on the capacitance recorded for the particular mass in addition to the full cell voltage [15]. Thus, it is eminent to use effective and efficient techniques to synthesize nano-scaled materials having adequate porosity for a better capacitance.

* Corresponding author.

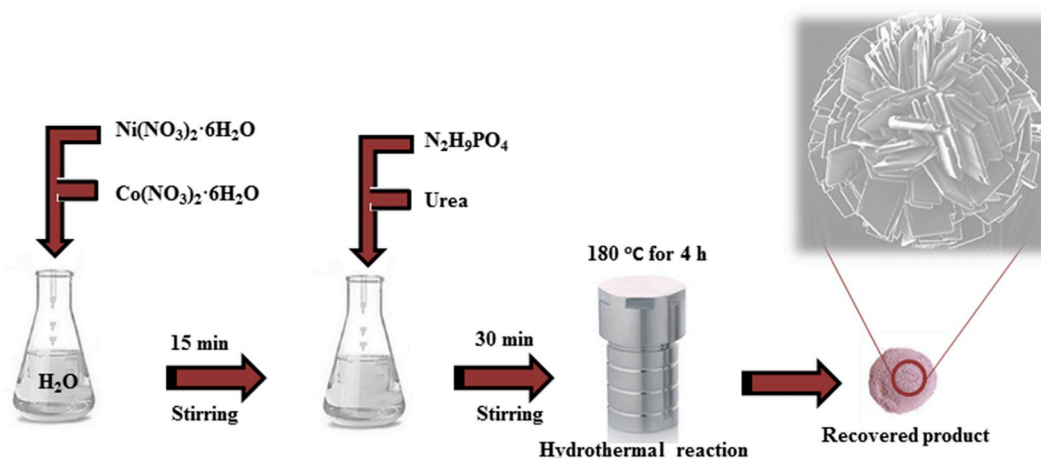
E-mail address: ncholu.manyala@up.ac.za (N. Manyala).

<https://doi.org/10.1016/j.compositesb.2019.106953>

Received 8 December 2018; Received in revised form 10 May 2019; Accepted 27 May 2019

Available online 29 May 2019

1359-8368/© 2019 Elsevier Ltd. All rights reserved.

Scheme 1. Scheme of the synthesis route of $\text{NiCo}(\text{PO}_4)_3$.

The development of hybrid/asymmetric electrochemical capacitor using a porous carbon based materials as positive electrodes and pseudocapacitive electrode materials as negative electrode which can proficiently increase the potential window between the carbon and the pseudocapacitive to increase the overall cell energy density since the energy density is directly proportional to the capacitance and voltage squared [16]. Carbon based material are ideal for EDLC because of their fascinating properties as controlled porosity, high specific surface area and high ionic conductivity. Despite having relatively high surface areas, the charges are generally stored substantially on the surface. The consequences of this is that the porous carbon materials suffer from lower specific capacitance and energy density [17]. Due to their high specific capacitance/capacity, but poor stability and electrical conductivity, conducting polymers and transition metal oxides (TMOs) have been widely investigated. Common example of TMOs reported are cobalt oxide (Co_3O_4), ruthenium oxide (RuO_2), and nickel oxide (NiO) [18–20]. RuO_2 material has fast responses of redox reaction mobility. Yet, it has a wide quasi-rectangular cyclic voltammetry (CV) shape owing to distinctive properties such as fast ions mobility, fast redox reactions, high specific surface area and also high conductivity. RuO_2 possess a high capacitance; nevertheless, the application of RuO_2 is limited because of the high cost. Thus, a lot of research has been done looking for suitable replacement for RuO_2 with low cost [21]. Recently, some studies have established bimetallic oxides in the field of energy storage, which could be an effective way because it considers the advantages of both individual metals which reflect on the enhancement of the combination. For instance, Prasankumar et al. studied the possibilities of improving the low electrical conductivity of MnO_2 by incorporating ZnO to form Mn/Zn bimetallic oxide using the microwave-assisted method. The fabricated Mn/Zn bimetallic oxide achieved a specific capacitance of 251 F g^{-1} at 0.5 A g^{-1} in 1 M KOH electrolyte. After 5000 charge-discharge cycles, 250 F g^{-1} still retained [22]. Layered phosphates materials have also attracted attention from the researchers since 1987 and have shown outstanding performance in catalysis, ion exchange, proton conductivity, interface chemistry, photochemistry, and materials science [23]. Furthermore, transition metal phosphates like nickel/cobalt phosphates can work as potential electrodes for adsorbents, magnetic materials and rechargeable batteries [24–26]. PO_4 polyhedra with different structures and morphologies have outstanding electronic and magnetic properties and have shown significant improvement as electrodes for SCs [27–29]. For example, Bing et al. reported ultrathin nickel–cobalt phosphate 2D nanosheets that could be operated up to 0.4 V in three-electrode configuration and 1.2 V in an asymmetric nickel–cobalt phosphate//activated carbon configuration using 3.0 M KOH electrolyte. A capacitance of 1132.5 F g^{-1} was claimed while capacity in (mAh g^{-1}) is preferable in

this type of nonlinear charge-discharge (GCD) materials [30]. Yaoning et al. investigated 1D and 2D nanowire and nanosheet of amorphous cobalt phosphate respectively reporting a specific capacitance of 1174 F g^{-1} at 2 A g^{-1} was reported using 3 M KOH in 3-electrode setup [31]. In order to develop new approaches to make phosphate-based materials, some attempts have been made. Thus, synthesis of phosphate-based nanomaterials combining two properties of absolute redox and pseudocapacitive signature with well-defined morphology remains an active field to be explored. From the family of transition metal phosphate, cobalt phosphate is considered a fascinating electrochemical pseudocapacitor material and nickel phosphate is a potential interest as faradaic material [32,33]. Combining these two materials resulted in an efficient pseudocapacitive behavior with excellent performance. It is highly desirable to make stable Ni-Co phosphate nanomaterials and increase the conductivity with graphene. This is due to the fact that graphene exhibits exceptional thermal and electrical conductivity, strength, high specific surface area up to $2675 \text{ m}^2 \text{ g}^{-1}$ and high intrinsic capacitance properties [34]. Therefore, it is expected that $\text{NiCo}(\text{PO}_4)_3/\text{GF}$ with nanoplatelets morphology will have much improved electrochemical results. Thus, we report the synthesis of $\text{NiCo}(\text{PO}_4)_3$ and $\text{NiCo}(\text{PO}_4)_3/\text{GF}$ composite combining the rich redox reaction of nickel phosphate and pseudocapacitive activity of cobalt phosphate. $\text{NiCo}(\text{PO}_4)_3/\text{GF}$ composite present a high specific capacity of 86.4 mAh g^{-1} at a specific current of 1 A g^{-1} . An asymmetric device fabricated using the $\text{NiCo}(\text{PO}_4)_3/\text{GF}$ composite as a positive, and AC as negative electrode exhibited a high energy density of 34.8 Wh kg^{-1} and power density of 377 W kg^{-1} at 0.5 A g^{-1} , accompanied with excellent cycling stability (95% capacity retention after 10000 charge-discharge cycles at 8 A g^{-1}).

2. Materials and methods

2.1. Synthesis of graphene foam (GF)

Graphene foam (GF) was synthesized via chemical vapor deposition (CVD) system has used. Nickel foam (from Alantum, Munich, Germany with an areal density of 420 g m^{-2} and 1.6 mm thickness) was used as a substrate. The procedures of growth of graphene foam on the nickel foam substrate were reported in our previously published work [35]. The procedures were as follow: The nickel foam (NF) was inserted directly into the quartz tube and controlled in the center of the CVD system. The system was heated up to $1000 \text{ }^\circ\text{C}$ for 1 h for complete removal of any possible impurities and other functional groups from the surface of NF. This was done under an H_2 : Ar gasses with the ratio of 200:300 sccm, after that methane (CH_4) at a flow rate of 10 sccm was passed through the tube for 10 min . After 10 min the tube was rapidly cooled to allow the graphene to precipitate on the surface of NF. After

the CVD system has cooled to room temperature the nickel-graphene foam was taken and the nickel was etched using 3.0 M HCl after which the graphene foam washed several times with deionized water and dried at 70 °C.

2.2. Hydrothermal synthesis of $\text{NiCo}(\text{PO}_4)_3$ and $\text{NiCo}(\text{PO}_4)_3/\text{GF}$ composite

The hydrothermal method was used for the synthesis of pristine $\text{NiCo}(\text{PO}_4)_3$ nano-platelets. The procedures for the production of the nano-platelets are shown in Scheme 1. First, 1.05 g, 1.06 g, 0.3 g and 0.1 g of nickel nitrate hexahydrate ($\text{Ni}(\text{NO}_3)_2 \cdot 6\text{H}_2\text{O}$), cobalt nitrate hexahydrate ($\text{Co}(\text{NO}_3)_2 \cdot 6\text{H}_2\text{O}$), ammonium phosphate ($\text{N}_2\text{H}_5\text{PO}_4$) and urea

($\text{CH}_4\text{N}_2\text{O}$) respectively were mixed together in deionized water (60 ml) and allowed to homogenize by stirring for 45 min. The homogenized solution was then transferred into a Teflon-lined, stainless-steel autoclave for the production of the nano-platelets. After 4 h reaction in an electric oven at 180 °C, the samples were removed from the oven and left to cool naturally to room temperature. The samples were then filtered and washed repeatedly using deionized water and placed in an electric oven at 60 °C to dry overnight. In order to synthesize $\text{NiCo}(\text{PO}_4)_3/\text{GF}$ composite, the same procedure mentioned above was followed with the addition of 40 mg graphene foam. An optimization process was carried out where 40 mg GF was the optimum mass for the best electrochemical performance when compared to 20 and 60 mg of GF respectively (see Fig. S1).

2.3. Synthesis of AC

The activated carbon used as the negative electrode in the hybrid configuration was prepared using polyvinyl alcohol (PVA) to provide carbon as demonstrated in our previous work [36]. The addition of a little concentration of lithium hydroxide was introduced to improve the conductivity of the activated carbon, through the conventional chemical activation using potassium hydroxide (KOH) as the active agent for the production of porous carbon that is desired. Briefly, PVA hydrogel was synthesized via the hydrothermal process. Typically, 10 g of polyvinyl alcohol was dissolved in 100 ml of water to obtain a clear gel solution, to this, a 0.1 M LiOH was added and stirred to obtain a homogeneous solution, and then transferred into a Teflon-lined autoclave system operated at 180 °C for 24 h. The resulting hydrogel was soaked in a 1:1 (KOH/hydrogel) ratio for 24 h followed by drying and heat treatment at 700 °C under argon flow for 2 h to obtain the desired activated carbon (AC) material. In order to remove the remained unreacted KOH from the AC, 3 M HCl was used for washing and finally, the AC flushed with deionized water and kept to dry at 60 °C overnight.

2.3.1. Materials characterization

X-ray diffraction was used for structure analysis in the range $2\theta = 10^\circ - 70^\circ$. The specification of the instrument is as follows: XPERT-PRO diffractometer (Analytical BV, the Netherlands) with $\theta/2\theta$ geometry and a counting time of 5.240 s per step. Qualitative phase examination of the samples was directed with the X'Pert Highscore search-match software at room temperature using $\text{Co K}_{1\alpha}$ ($\lambda = 0.178897 \text{ nm}$). X-ray photoelectron spectroscopy (XPS) measurements of the samples were conducted using a Physical Electronics VersaProbe 5000 spectrometer operating with a 100 mm monochromatic Al-K α exciting source. A WITec Confocal Raman Microscope (WITec alpha300 R, Ulm, Germany) with a 532 nm laser wavelength, 4 mW laser power and 120-s spectral acquisition time was used for Raman analysis. The SEM images were obtained on a Zeiss Ultra Plus 55 field emission scanning electron microscope (FE-SEM) (Carl Zeiss, Oberkochen, Germany) operated at an accelerating voltage of 2.0 kV. The elemental composition was carried out using Energy dispersive Spectroscopy (EDS), Oxford Instrument (INCA 4.11 software). Surface area was obtained by the Brunauer–Emmett–Teller (BET) technique from the N_2 adsorption isotherm.

To fabricate the electrodes, 80% of the active material was mixed with 10% carbon black and 10% polyvinylidene difluoride (PVDF) as a binder. A 1-methyl-2-pyrrolidinone (NMP) was later added to make slurry. After perfect mixture of the material with the NMP, the paste was coated on the nickel foam with a diameter of 1 cm^2 and dried at 70 °C overnight to evaporate the NMP. The masses of the electrode materials were about 3.0 mg each. The electrochemical measurements were carried out in a 3-electrode system using Ag/AgCl (3 M KCl saturated) and glassy carbon as the reference electrode and counter electrode respectively. A 1.0 M KOH aqueous electrolyte was used in this experiment in potential range of 0–0.45 V vs Ag/AgCl . A coin cell type CR2025 was used to assemble the hybrid supercapacitor. Different negative and

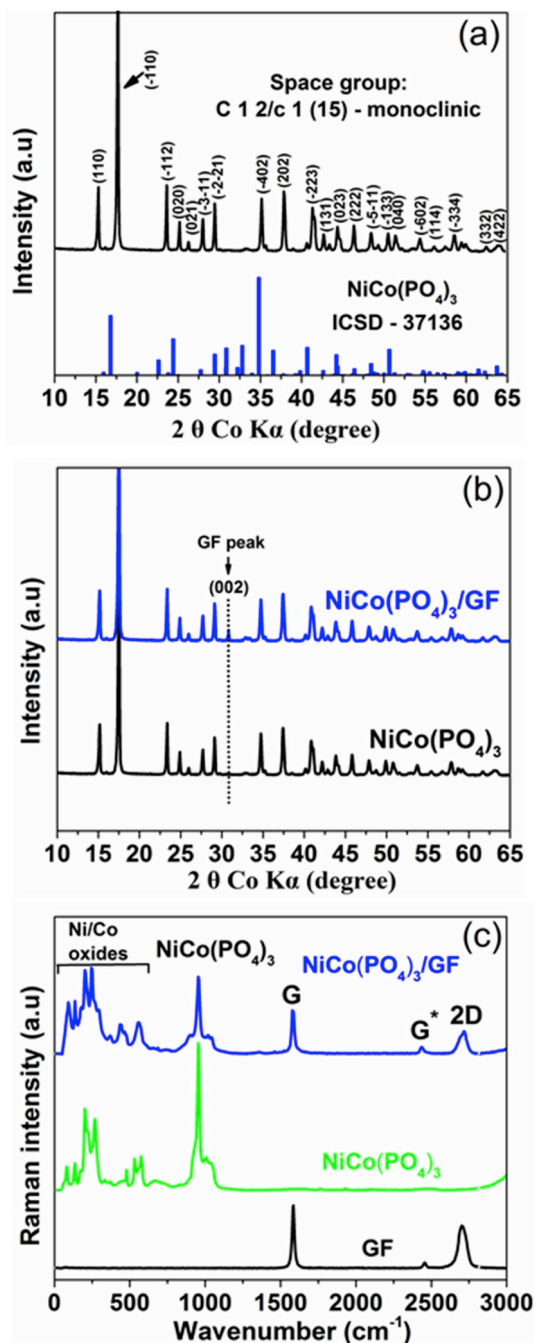


Fig. 1. (a) XRD patterns of the as-prepared samples with $\text{NiCo}(\text{PO}_4)_3$ (ICSD No. 37136), (b) XRD pattern of as-prepared $\text{NiCo}(\text{PO}_4)_3$ and $\text{NiCo}(\text{PO}_4)_3/\text{GF}$ composite and (c) Raman spectrum of GF, $\text{NiCo}(\text{PO}_4)_3$ and $\text{NiCo}(\text{PO}_4)_3/\text{GF}$.

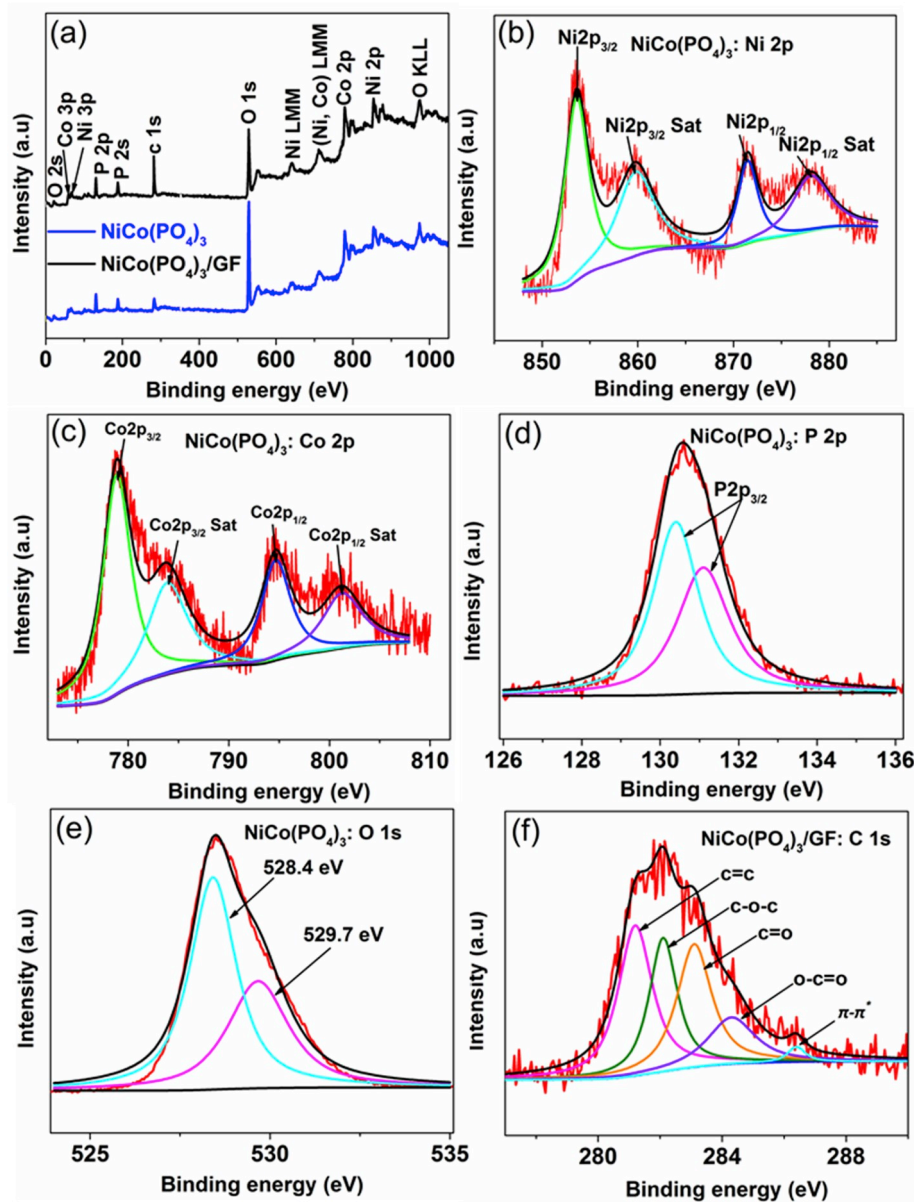


Fig. 2. (a) XPS survey spectra of $\text{NiCo}(\text{PO}_4)_3$ and $\text{NiCo}(\text{PO}_4)_3/\text{GF}$, high resolution spectra of (b) Ni 2p, (c) Co 2p, (d) P 2p, (e) O 1s for pristine $\text{NiCo}(\text{PO}_4)_3$ and (f) C 1s for $\text{NiCo}(\text{PO}_4)_3/\text{GF}$.

positive materials were used and the microfiber glass filter paper used to separate the two electrodes. Cyclic voltammetry (CV) was applied to confirm the cell-type while Galvanostatic charge-discharge (GCD) was applied for further confirmation of the cell-type and also to calculate the cell capacity. Both the CV and GCD were carried out in a cell potential ranging between 0.0 and 1.4 V. The CV was tested at a scan rate of 5, -100 mV s^{-1} ; the GCD was tested in a specific current of 0.5, -10 A g^{-1} . The impedance of the hybrid was also investigated with electrochemical impedance spectroscopy (EIS) in range 100 kHz to 0.01 Hz with zero potential amplitude using a Bio-logic VMP-300 potentiostat (Knoxville, US) driven by the EC-lab software. The specific capacity (C_s) of $\text{NiCo}(\text{PO}_4)_3/\text{GF}$ was estimated from the GCD profile using the following equation [33]:

$$C_s (\text{mAh g}^{-1}) = \frac{I_d \Delta t}{3.6} \quad (1)$$

where I_d is the specific current (A g^{-1}), and Δt is the discharge time (s).

For the hybrid device, the $\text{NiCo}(\text{PO}_4)_3/\text{GF}$ composite was considered

as positive and the AC as negative electrodes respectively. The quantity of the charge in both positive electrode (Q_+) and negative electrode (Q_-) were balanced using the following formulas:

$$Q^+ = Q^- \quad (2)$$

$$m_+ + I_{d(+)} \Delta t_+ = m_- I_{d(-)} \Delta t_- \quad (3)$$

where Q_+ and Q_- represent negative and positive charges respectively, m_+ and m_- represent the active masses of the positive and negative respectively. The mass ratio ($m_+:m_-$) recorded for the positive and negative was found to be 1:1.6 at the specific current of 1 A g^{-1} , consequently the active masses of the positive and the negative were 2.1 and 3.4 g respectively. The energy density, E_d (Wh kg^{-1}) and the power density, P_d (W kg^{-1}) were calculated from the GCD curves using the following equations:

$$E_d (\text{Wh kg}^{-1}) = \frac{i}{3.6(m_+ + m_-)} \int V dt \quad (4)$$

$$P_d(W.kg^{-1}) = 3600 \frac{E_d}{\Delta t} \quad (5)$$

where i is the applied current (mA), m is the total mass of the active material (mg), $\int Vdt$ is the area under the discharge curve of the device, and Δt is the discharge time (s).

3. Results and discussion

Fig. 1(a) shows the XRD pattern of the pure $NiCo(PO_4)_3$ sample with a predominant diffraction peak at $\sim 17^\circ$ corresponding to (-110) plane. The presence of strong and narrow diffraction peaks confirms the crystal state of the sample, which indicates the good crystallinity of the material. The indexation of the diffraction peaks was done according to Crystal Structure Database (ICSD) card no. 37136 with a chemical formula $NiCo(PO_4)_3$, space-group C1 2/c 1 (15) - monoclinic and cell parameters $a = 11.718 \text{ \AA}$, $b = 8.267 \text{ \AA}$ and $c = 9.871 \text{ \AA}$. To study the structure and the crystallinity of $NiCo(PO_4)_3$ material, Visualization Molecular Structure (Diamond - Crystal) software was used [37]. Raman analysis of the graphene foam, $NiCo(PO_4)_3$ and $NiCo(PO_4)_3/GF$ is shown in Fig. 1(c). The pure graphene foam (GF) shows Raman signature of graphene with G-band at about 1586 cm^{-1} and 2D-band at about 2704 cm^{-1} respectively. These bands are attributed to the C–C vibration mode (G peak) and double resonance process (2D peak) of carbon [38]. A peak at about 2452 cm^{-1} is attributed to phonon dispersion to the double resonance scattering process in graphene, and this mode is usually referred to as G^* or $D + D^*$ [39]. The G, 2D and G^* peaks were also observed in $NiCo(PO_4)_3/GF$ composite with less intensity which shows the presence of GF in the composite and also the incorporation of GF into the matrix of $NiCo(PO_4)_3$. The strong peak at 953 cm^{-1} on the $NiCo(PO_4)_3$ pristine Raman spectrum is ascribed to the symmetric stretching and vibrational mode of PO_4^{3-} . The materials also show Raman mode at 95, 135, 205, 248, 442 and 556 cm^{-1} comparing with the literature these modes could be assigned to Ni-Co-O phases [40–42]. However it's difficult to refer to a specific phase that could be responsible for these vibrational modes [43]. The intensity ratio of the I_{2D}/I_G peaks in the composite spectrum was measured to be ~ 0.92 which confirms the GF used to make the composite was composed of few layers [44]. Fig. 1(b) shows the XRD pattern of the $NiCo(PO_4)_3$ and $NiCo(PO_4)_3/GF$ composite. It can be observed that with the introduction of GF the XRD pattern of the $NiCo(PO_4)_3/GF$ does not change, however, the peak (002) at about 30.85° appeared as result of GF in $NiCo(PO_4)_3/GF$ sample.

The surface chemistry of the $NiCo(PO_4)_3$ and $NiCo(PO_4)_3/GF$ was analyzed by XPS. Fig. 2(a) shows the wide scan XPS survey spectra of the pristine (blue) and composite (black) nickel cobalt phosphate samples which display the main elements (Ni 2p, Co 2p, P 2p, O 1s and C 1s) of the composition of the samples. The pristine sample shows atomic percentages of 15.11% Ni 2p, 16.14% Co 2p, 12.11% P 2p, 10.94% C 1s and 45.69% O 1s indicating the sample is predominantly composed of oxygen. The composite shows atomic percentages of 8.55% Ni 2p, 10.14% Co 2p, 9.72% P 2p, 36.52% O 1s and 35.52% C 1s suggests that the content of carbon is higher on the surface compared to the pristine. Interestingly, a surface of a composite sample can be expected to have a good electrical conductivity owing to the outstanding electrical conductivity of graphene.

Fig. 2(b), (c), (d), (e) and (f) show the high-resolution emission spectra of Ni 2p, Co 2p, P 2p, O 1s, and C 1s respectively. The binding energy peaks located at 853.67, 859.90, 871.49 and 878.16 eV in Fig. X (b) agree with Ni $2p_{3/2}$ and Ni $2p_{1/2}$ in addition to the satellite shakeup are assigned to the chemical state of Ni^{2+} and Ni^{3+} [45]. The binding energy peaks located at 778.95, 783.87, 794.74 and 801.34 eV in Fig. X (c) which agree with Co $2p_{3/2}$ and Co $2p_{1/2}$ in addition to the satellite shakeup are assigned to the chemical state of Co^{2+} and Co^{3+} [45]. In the P 2p spectrum, the binding energy peaks at 130.39 and 131.12 eV in Fig. X (d) are correspond to P–P and P–O bonds respectively [46]. Fig. 2

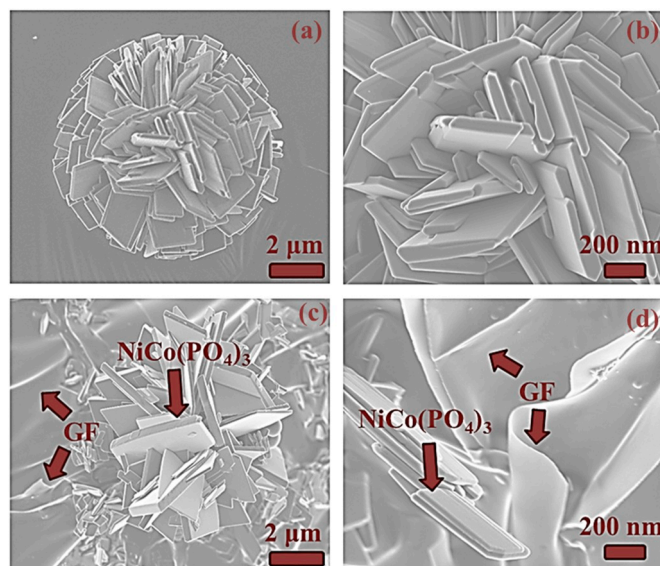


Fig. 3. (a and b) low and high magnification SEM images of pristine $NiCo(PO_4)_3$ and (c and d) low and high magnification SEM images of $NiCo(PO_4)_3/GF$ composite.

(e) shows the spectrum of O 1s with fitted peaks at 528.43 and 529.68 eV which could be ascribed to O 1s in (Ni–O), (Co–O) and P–O compounds [47].

Fig. 2(f) shows a C 1s spectrum of $NiCo(PO_4)_3/GF$ composite. The binding energy peaks at 281.19, 282.10, 283.12, 284.32 and 286.43 eV correspond to sp^2 C=C (graphene component), C–O–C, C=O, O–C=O (oxide components) and $\pi-\pi^*$ (satellite peak/electrons transition) bonding respectively. In this figure, all fitted peaks reveal the sp^2 hybridization property of GF, traces of oxygen content present in GF and the $\pi-\pi^*$ electrons transition which enhances the carbon to carbon bonds in graphene and confirms the high quality of GF [33].

The morphology of as-prepared $NiCo(PO_4)_3$ was observed using SEM and the result is presented in Fig. 3(a and b) at low and high magnification respectively. It is clearly observed from the figure that the sample is composed of nanosheets with different thicknesses assembled together to form a flower-like structure (Fig. 3(a)). The morphology of $NiCo(PO_4)_3/GF$ is also shown in Fig. 3(c and d) at low and high magnification. Similarly, the introduction of graphene did not alter the morphology of the material; rather the nanosheets are grown on the sheet of graphene as revealed in Fig. 3(d). It is realized that the nanosheets are well distributed on the graphene sheet surface signifying that $NiCo(PO_4)_3$ are homogeneously distributed on the surface of the graphene and attached to it. The EDS analysis was carried out to show the elemental composition of the pristine $NiCo(PO_4)_3$ and $NiCo(PO_4)_3/GF$ composite. The EDS analysis (see Fig. S1) confirmed the presence of Ni, Co, P, and O in the $NiCo(PO_4)_3$ and also C in $NiCo(PO_4)_3/GF$.

The nitrogen (N_2) gas sorption test was carried out to measure the achievable surface area and pore structure of the materials. Fig. 4(a) displays the N_2 isotherms and pore size distribution (PSDs) of the as-prepared $NiCo(PO_4)_3$. As perceived in Fig. 4(a) both samples establish a type III behavior with a H3-type hysteresis loop indicating materials containing both micropores and mesopores isotherm, which features convex to the X axes over its entire range attributed to the strong interaction between adsorbed molecules in slit-like pores [48]. The micropores are for the charge to be stored and ion adsorption whereas mesopores are channels permits the ions to move between the electrolyte and electrolyte/electrode interface. Fig. 4(b) displays the pore size distribution (PSDs) acquired with the Barrett-Joyner-Halenda (BJH) exploration in the range of 1–18 nm. The PSDs of both samples showed the existence of mesoporous and below 2 nm the shape of the graph indicates the presences of micropores. The specific surface areas

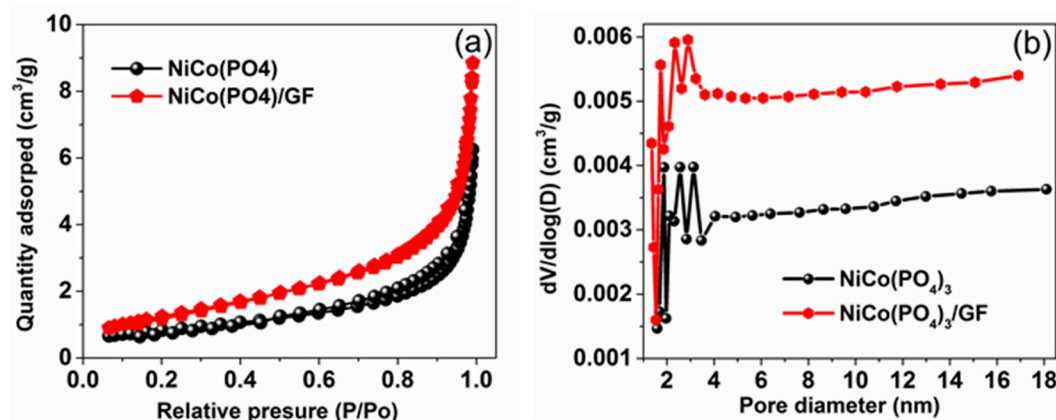


Fig. 4. (a). Study of N₂ adsorption-desorption measurement and (b) the BJH pore size analysis graphs estimated using isotherm desorption branch.

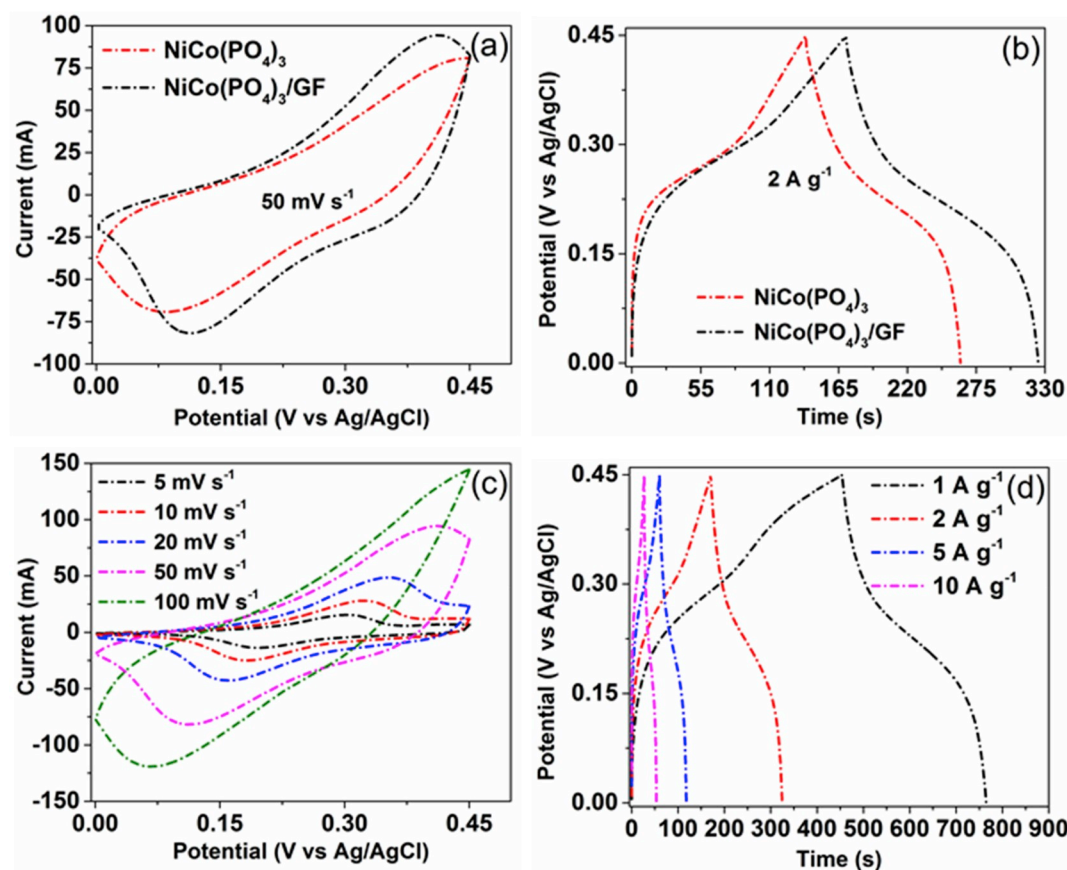


Fig. 5. (a) CV curves of pristine NiCo(PO₄)₃ and NiCo(PO₄)₃/GF composites measured at scan rate of 50 mV s⁻¹, (b) GCD curves of pristine NiCo(PO₄)₃ and NiCo(PO₄)₃/GF composites measured at 2 A g⁻¹, (c) CV curves of NiCo(PO₄)₃/GF composite at different scan rates and (d) GCD profile of NiCo(PO₄)₃/GF composite measured at different specific currents.

recorded for the pristine NiCo(PO₄)₃ and NiCo(PO₄)₃/GF composite were 2.9 m² g⁻¹ and 6.1 m² g⁻¹ respectively. The increase in the specific surface area can be accredited to the existence of graphene foam in the composite. Consequently, the electrochemical performance of the composite was significantly improved.

Fig. 5(a) shows the comparative CV profiles of the pristine and composite samples at a scan rate of 50 mV s⁻¹. As Observed from the CV curves (Fig. 5(a)), both pristine and composite materials reveal a faradaic shape with less intense peaks indicating a possible influence of nickel which is rich in redox reaction [33] and cobalt which depicts quasi-rectangular behavior [32]. Though, the difference of current

response in the CV curves is distinguished between NiCo(PO₄)₃ and NiCo(PO₄)₃/GF as NiCo(PO₄)₃/GF appearances a better current response demonstrating the significant impact of the graphene foam in the composite. The abovementioned outcomes that the graphene foam is a worthy medium for the NiCo(PO₄)₃ nanoplatelets to grow and synergize therefore resulting in improved surface area and conductivity which are essential for electrochemical properties [49]. Fig. 5(b) shows typical GCD profiles of NiCo(PO₄)₃ and NiCo(PO₄)₃/GF measured at 2 A g⁻¹. The longer discharge time of GCD curve was seen for NiCo(PO₄)₃/GF which was a further confirmation the results obtained from the CV curves (Fig. 4(a)).

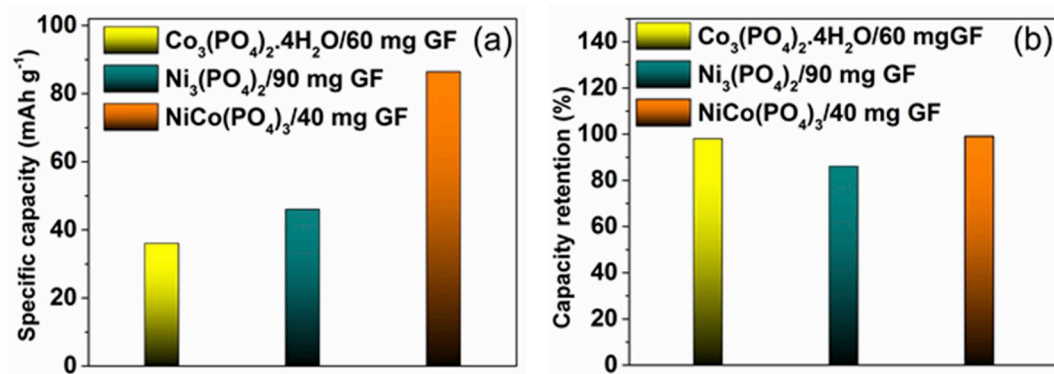


Fig. 6. (a) specific capacity comparison of $\text{Co}_3(\text{PO}_4)_2 \cdot 4\text{H}_2\text{O}/\text{GF}$, $\text{Ni}_3(\text{PO}_4)_2/90 \text{ mg GF}$ and $\text{NiCo}(\text{PO}_4)_3/\text{GF}$ calculated from GCD curves in 3-electrode configurations and (b) capacity retention comparison of $\text{Co}_3(\text{PO}_4)_2 \cdot 4\text{H}_2\text{O}/\text{GF}$, $\text{Ni}_3(\text{PO}_4)_2/90 \text{ mg GF}$ and $\text{NiCo}(\text{PO}_4)_3/\text{GF}$ in 3-electrode configuration.

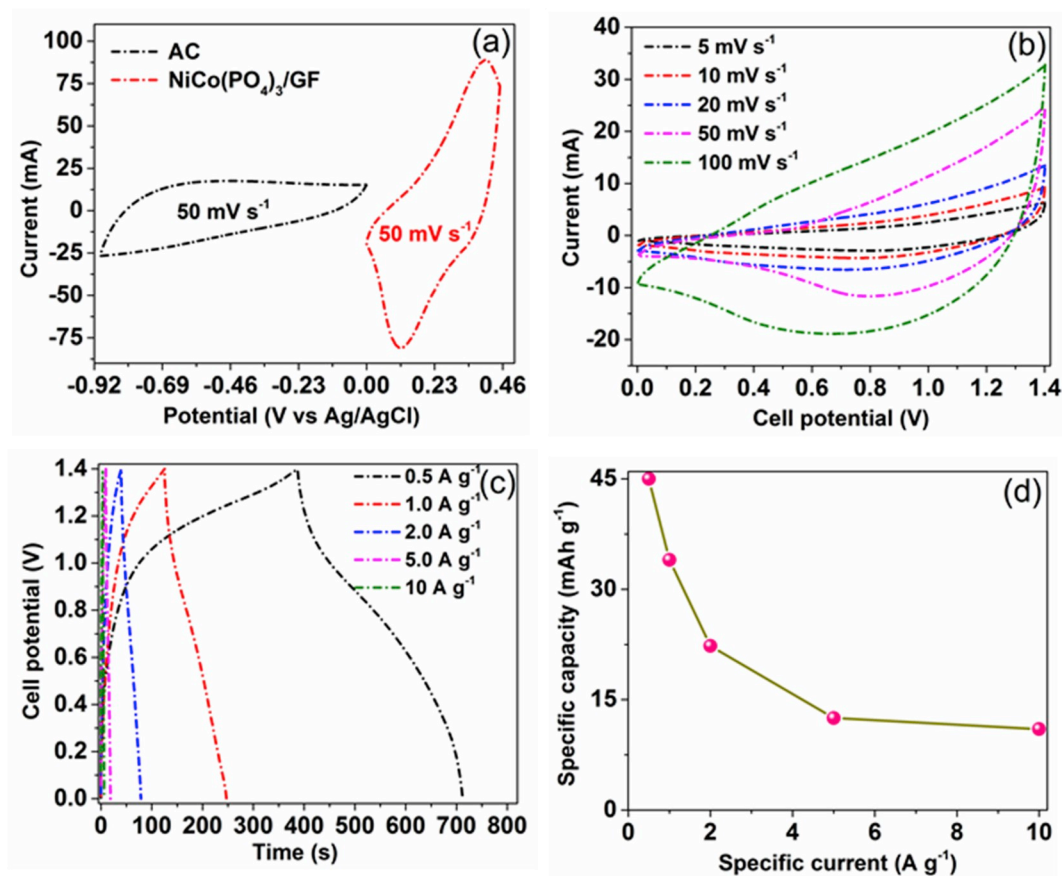


Fig. 7. (a) CV profile of $\text{NiCo}(\text{PO}_4)_3/\text{GF}$ and AC measured at 50 mV s^{-1} in 3-electrode configuration, (b) CV profile of the $\text{NiCo}(\text{PO}_4)_3/\text{GF} // \text{AC}$ hybrid device measured at different scan rates within 0–1.4 V, (c) GCD profile of the $\text{NiCo}(\text{PO}_4)_3/\text{GF} // \text{AC}$ hybrid device measured at a different specific current within 0–1.4 V and (d) a specific capacity of the $\text{NiCo}(\text{PO}_4)_3/\text{GF} // \text{AC}$ hybrid device at different specific currents calculated from GCDs in (c).

Since the composite has a better capacitive response, a detailed electrochemical assessment was made on the $\text{NiCo}(\text{PO}_4)_3/\text{GF}$. Fig. 5(c) shows the cyclic voltammograms of $\text{NiCo}(\text{PO}_4)_3/\text{GF}$ composite at scan rates ranging from 5 to 100 mV s^{-1} at a fixed potential of 0.0–0.45 V vs Ag/AgCl. All the CV profiles had the same shape and the current response was found to increase as the scan rate increases from 5 to 100 mV s^{-1} suggesting the reversibility of fast charge-discharge process. The GCD curves at different specific current from 1 to 10 A g^{-1} in a potential range of 0.0–0.45 V are also shown in Fig. 5(d), revealing a non-linear potential-time relation which is consistent with the CV curves in Fig. 5(c).

Fig. 6(a) displays the specific capacity of the $\text{Co}_3(\text{PO}_4)_2 \cdot 4\text{H}_2\text{O}/60 \text{ GF}$, $\text{Ni}_3(\text{PO}_4)_2/90 \text{ mg GF}$ and $\text{NiCo}(\text{PO}_4)_3/40 \text{ mg GF}$ calculated from the GCD curves of the 3-electrode measurements. It worth mentioning that the data used to compare our present work in Fig. 5(a and b) were results from our previously published work of $\text{Co}_3(\text{PO}_4)_2 \cdot 4\text{H}_2\text{O}/60 \text{ GF}$ and $\text{Ni}_3(\text{PO}_4)_2/90 \text{ mg GF}$ respectively [32,33]. It is observed that the combination of the high capacity materials ($\text{Ni}_3(\text{PO}_4)_2$) with pseudocapacitive material ($\text{Co}_3(\text{PO}_4)_2$) resulted in pseudocapacitive properties of the $\text{NiCo}(\text{PO}_4)_3/\text{GF}$ and also increased the specific capacity of the material as a result of the synergy between these two materials and the graphene foam. Cyclic stability is often an important parameter in the practical

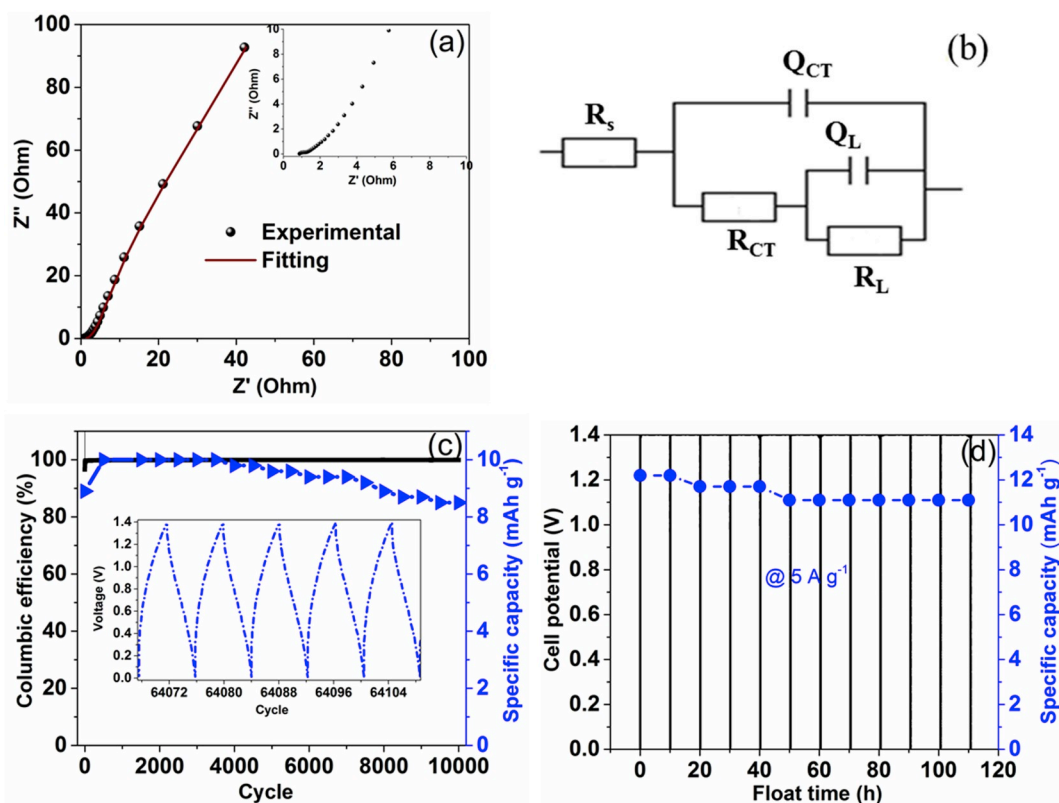


Fig. 8. (a) the Nyquist plot of the hybrid device, (b) an equivalent map applied for EIS data fitting in a $\text{NiCo}(\text{PO}_4)_3/\text{GF}//\text{AC}$ hybrid device, (c) double Y plot illustrating coulombic efficiency and specific capacity versus cycle number of $\text{NiCo}(\text{PO}_4)_3/\text{GF}//\text{AC}$ hybrid device at specific current of 8 A g^{-1} (the inset is some GCD cycles) and (d) double Y plot illustrating the cell potential and the specific capacity versus float time of $\text{NiCo}(\text{PO}_4)_3/\text{GF}//\text{AC}$ hybrid device.

application of supercapacitors. Fig. 6(b) shows the comparison of capacity retention of $\text{Co}_3(\text{PO}_4)_4 \cdot 4\text{H}_2\text{O}/\text{GF}$ and $\text{Ni}_3(\text{PO}_4)_2/90 \text{ mg GF}$ to the current work $\text{NiCo}(\text{PO}_4)_2/\text{GF}$ measured for 3-electrode configurations. The retention of the $\text{NiCo}(\text{PO}_4)_2/\text{GF}$ was observed to be improved as compared to the individual $\text{Ni}_3(\text{PO}_4)_2$ which lacks stability because of the redox reaction that occurs at the electrode, much similar to pseudocapacitive $\text{Co}_3(\text{PO}_4)_4 \cdot 4\text{H}_2\text{O}/\text{GF}$ [50].

In order to fully explore the electrochemical performance of $\text{NiCo}(\text{PO}_4)_3/\text{GF}/\text{AC}$ electrode as both positive and negative electrodes, a hybrid device (scheme in Fig. S4) is fabricated using 1 M KOH as electrolyte. Fig. 7(a) shows the CV curves of both $\text{NiCo}(\text{PO}_4)_3/\text{GF}$ and AC electrodes at a scan rate of 50 mV s^{-1} in three-electrode measurement. Since the $\text{NiCo}(\text{PO}_4)_3/\text{GF}$ electrode has a potential range of $0.0\text{--}0.45 \text{ V}$ and AC has a potential range of $-0.9\text{--}0.0 \text{ V}$ vs Ag/AgCl , the CV curves of $\text{NiCo}(\text{PO}_4)_3/\text{GF}//\text{AC}$ a hybrid device is expected to extend its potential up to 1.4 V . The device showed that as the cell potential approaches 1.4 V the currents in the positive and negative electrodes do not show any form of hydrogen and oxygen evolution respectively which should be witnessed if the cell potential is exceeded as shown in Fig. 6(b). The CV curves of the device at different scan rates from 5 to 100 mV s^{-1} are shown in Fig. 7(b). It can be seen that the CV curves at different scan rates display a quasi-rectangular profile as result of a collective influence of EDLC (AC) and faradaic ($\text{NiCo}(\text{PO}_4)_3/\text{GF}$) activities which is a distinctive performance of hybrid supercapacitor. Furthermore, the GCD profiles at different specific currents from 0.5 to 10 A g^{-1} (Fig. 7(c)) expresses potential stages which approve the quasi-rectangular manner of the hybrid device as projected by CV curves (Fig. 7(b)). Because of the device displays typically nonlinear characteristics, the specific capacity of the device was considered from the GCD profiles using equation (1) and found to be $45, 34, 22.3, 12.5$ and 11 mAh g^{-1} at specific currents of $0.5, 1.0, 2.0, 5.0$ and 10 A g^{-1} respectively. From Fig. 7(d), one can visibly see that there is a relatively fast drop in specific capacity as the

specific current increases. This is owed to the restricted drive of ions by dispersion at high specific current, which could only access the material on active surface [51].

Fig. 8(a and b) present the experimental data plotted together with fitting data and also the circuit used for fitting the EIS. In order to fit the EIS data, Z fit software which is driven by EC-lab V 10.40 was used [52]. In the equivalent circuit (Fig. 8(b)), R_s represents the series resistance. The R_{CT} and Q_{CT} describe the rate of resistance and the electrochemical faradaic activity that might take place at the electrode/electrolyte interface [53]. Q_L and R_L represent the capacitance and resistance associated with electrical double layer capacitance. The equivalent series resistance (R_s) is in series with the constant phase element Q_{CT} and also charge transfer resistance R_{CT} . The ideal supercapacitor shows a vertical line close to low-frequency area which is almost parallel to Y-axis giving a mass capacitance Q_L . The hybrid device in the current case shows a slight deviance from this ideal behavior which mainly refers to leakage resistance R_L arising from the faradaic charge transfer process [54]. In the corresponding circuit, R_L is in parallel to the Q_L , all of which are in series with R_s . The values of R_s and R_{CT} for the hybrid devices were estimated from the inset to Fig. 8(a) are 0.86Ω and 0.4Ω respectively. Fig. 8(c) demonstrates the long-term cyclic stability of the hybrid device which was conducted under a constant charge-discharge at 5 A g^{-1} for 10000 cycles. A 99% coulombic efficiency and 95.5% of its initial capacity retained revealing a good electrochemical stability of the hybrid device and suggesting a superior cyclic performance for the electrode materials. Fig. 8(d) displays, the progression of hybrid cell capacity with floating over a time of 110 h at a specific current of 5 A g^{-1} , the hybrid device was exposed to a maximum operating cell potential (1.4 V) for 110 h and the capacity estimated every 10 h continuously. From Fig. 8(d), it is evident that the cell potential is stable within this cell potential and time with a capacity loss of $\sim 9\%$. This excellent cycling stability of the hybrid device could be

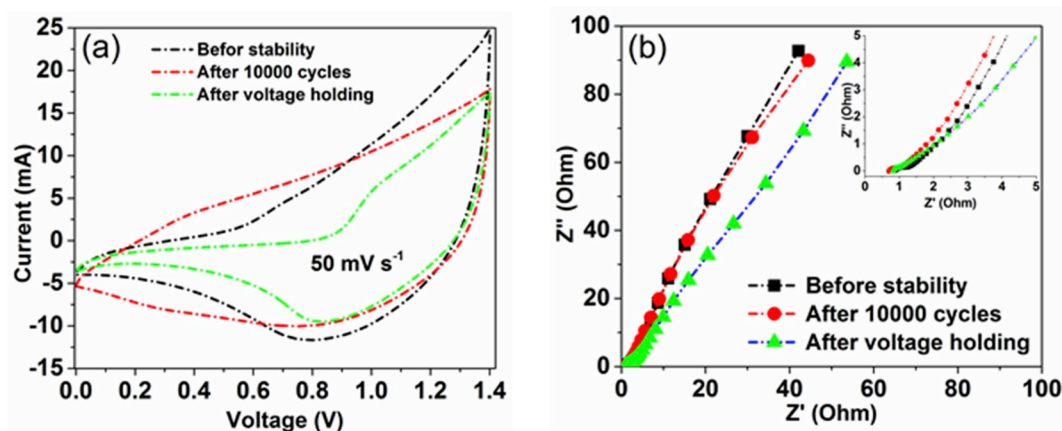


Fig. 9. (a) CV curves of the NiCo(PO₄)₃/GF//AC hybrid device before, after 10000 cycles and after voltage holding and (b) Nyquist plot of the NiCo(PO₄)₃/GF//AC hybrid device before, after 10000 cycle and after voltage holding.

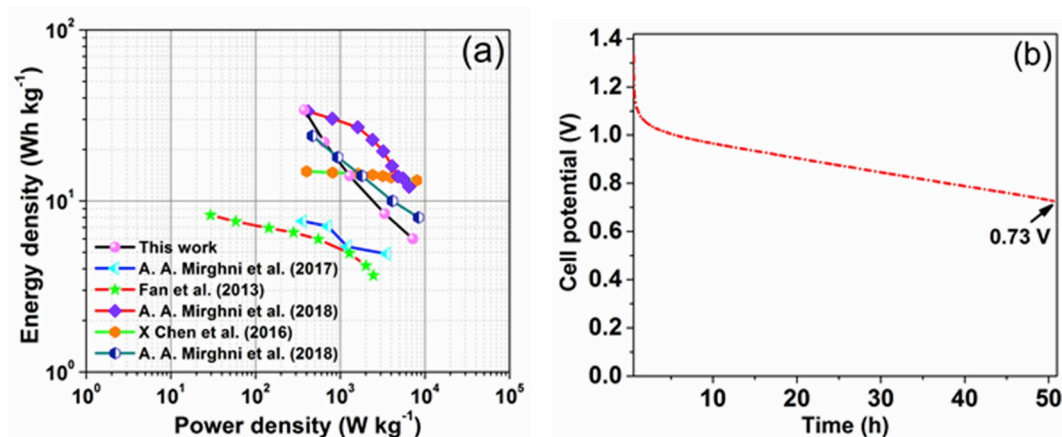


Fig. 10. (a) Ragone plot of the NiCo(PO₄)₃/GF//AC hybrid devices and other phosphate materials reported in literature and (b) Self-discharge of NiCo(PO₄)₃/GF//AC hybrid devices.

ascribed to the structure of NiCo(PO₄)₃ which is chemically stable demonstrating good and promising electrochemical performance.

Further evaluation of the cell before and after 10000 cycles and after voltage holding testing was carried out. Fig. 9(a) shows CV curves of the hybrid device before, after 10000 cycles and after voltage holding at 50 mV s⁻¹. The CV curves in Fig. 9(a) show that after 10000 cycles, the change in CV shape observed is almost negligible implies that there was no change in the structure of the material. Moreover, the area under CV curves before stability and after 10000 cycles remained almost the same. After subjecting the hybrid cell to a voltage holding of over 110 h, it can be observed that the device's current response of the CV curves slightly decreased, which can be correlated to the increased resistance as a result of over consumption of some of the active material which leads to consequent capacity loss [55,56]. This is in agreement with the result reported in Fig. 8(b). The Nyquist plots before, after 10000 cycles and after voltage holding test of over 110 h are presented in Fig. 9(b) revealing almost no change in the values of the series resistance R_s (see inset in Fig. 9(b)) which is an evidence of relaxed movement of the charge within the electrolyte. The R_s values of the hybrid device before stability, after 10000 cycles and after voltage holding were estimated to be 0.86 Ω , 0.71 Ω and 0.82 Ω respectively, while the R_{CT} were 0.4 Ω , 0.48 Ω and 0.33 Ω respectively. In the low-frequency region, the hybrid device shows a slight deviation from the ideal capacitive nature particularly after voltage holding which is ascribed to a leakage resistance, R_L arising from the faradaic charge transfer process. This is further confirmation to what observed in Fig. 9(a).

To evaluate the practical application of the SCs devices, specific energy density and power density are good factors to examine. Good SCs are expected to give considerable and comparable values of energy and power densities. Fig. 10(a) shows the Ragone plot of the NiCo(PO₄)₃/GF//AC hybrid device and the results of other works reported in the literature. As shown, the NiCo(PO₄)₃/GF//AC hybrid device recorded the highest energy density of 34.8 Wh kg⁻¹ and power density of 377 W kg⁻¹ at 0.5 A g⁻¹ which is superior to those reported in the literature [35,57,58]. Noticeably, compared to our recently published work, the energy and power densities of the NiCo(PO₄)₃/GF//AC hybrid device is superior to the values in Co₃(PO₄)₂/GF//C-FP and less than the values in Ni₃(PO₄)₂/90 mg GF//C-FP respectively [32,33]. This is due to the synergy of NiCo(PO₄)₃/GF as a combination of pseudocapacitive signature of Co₃(PO₄)₂/GF and highly redox reaction of Ni₃(PO₄)₂/GF. Another factor of stability of the electrode materials in SCs is self-discharge. Fig. 10(b) shows the NiCo(PO₄)₃/GF//AC hybrid device at room temperature. A short time swift fall of the cell potential is observed at the beginning of the self-discharge which is mainly because of the elemental breakdown of the water in the water-based electrolyte. Therefore 0.73 V was maintained after 50 h proposing encouraging material as future electrode for supercapacitors.

4. Conclusion

In summary, nanoplatelets morphology of the monoclinic structure of NiCo(PO₄)₃ was prepared via the hydrothermal processes. The

electrochemical performance of $\text{NiCo}(\text{PO}_4)_3$ was enhanced by exposing the graphene into the matrix of the material. The electrochemistry behind CV profile as well as GCD profile through the assessment implies that the capacity of $\text{NiCo}(\text{PO}_4)_3/\text{GF}$ composite was enhanced to 86.4 mAh g^{-1} as compared with the pristine $\text{NiCo}(\text{PO}_4)_3$ where the specific capacity was 64 mAh g^{-1} . This is essentially due to the synergistic effect between the conductive GF and $\text{NiCo}(\text{PO}_4)_3$ resulting in easing the mobility of the ions within the electrolyte. The hybrid electrochemical capacitor device fabricated using $\text{NiCo}(\text{PO}_4)_3$ as a positive electrode material and AC as negative material attained values of energy density and power density of 34.8 Wh kg^{-1} and 377 W kg^{-1} respectively at a specific current of 0.5 A g^{-1} . The hybrid device examined for a long-term cyclability over 10000 GCD cycles and interestingly 95% capacity was retained at a specific current of 8.0 A g^{-1} . The hybrid device also displayed excellent stability of 90% after 110 h voltage holding. Thus, $\text{NiCo}(\text{PO}_4)_3$ composite is a great potential candidate in energy storage application. These abovementioned electrochemical results of $\text{NiCo}(\text{PO}_4)_3$ almost lie in-between the values of the individual nickel phosphate and cobalt phosphate asymmetric devices respectively [32,33].

Acknowledgements

This work is based on research supported by the South African Research Chairs Initiative (SARChI) of the Department of Science and Technology and the National Research Foundation of South Africa (Grant No. 61056). Any opinion, finding and conclusion or recommendation expressed in this material is that of the author(s) and the NRF does not accept any liability in this regard. Abdulmajid A. Mirghni acknowledges the financial support from the University of Pretoria, the NRF through the SARChI in Carbon Technology and Materials, and also Al Fashir University, Sudan.

Appendix A. Supplementary data

Supplementary data to this article can be found online at <https://doi.org/10.1016/j.compositesb.2019.106953>.

References

- [1] Wei W, Cui X, Ivey DG. Manganese oxide-based materials as electrochemical supercapacitor electrodes. *Chem Soc Rev* 2011;40:1697–721.
- [2] Shrivastava A, Gupta S. Review on super capacitor-battery based hybrid energy storage system for PV application. *IJAEMS* 2017;4:378–81.
- [3] Ibrahim H, Ilinca A, Perron J. Energy storage systems — characteristics and comparisons. *Renew Sustain Energy Rev* 2008;12:1221–50.
- [4] Lopes H, Garde R, Fulli G, Kling W, Pecos J. Characterisation of electrical energy storage technologies. *Energy* 2013;53:288–98.
- [5] Prasankumar T, Karazhanov S, Jose SP. Three-dimensional architecture of tin dioxide doped polypyrrole/reduced graphene oxide as potential electrode for flexible supercapacitors. *Mater Lett* 2018;221:179–82.
- [6] Chu A, Braatz P. Comparison of commercial supercapacitors and high-power lithium-ion batteries for power-assist applications in hybrid electric vehicles I. Initial characterization. *J Power Sources* 2002;112:236–46.
- [7] Conway BE. Transition from “supercapacitor” to “battery” behavior in electrochemical energy storage. *J Electrochem Soc* 1991;138:1539–48.
- [8] Du Pasquier A, Plitz I, Menocal S, Amatucci G. A comparative study of Li-ion battery, supercapacitor and nonaqueous asymmetric hybrid devices for automotive applications. *J Power Sources* 2003;115:171–8.
- [9] Balducci A, Dugas R, Taberna PL, Simon P, Plee D, Mastragostino M, et al. High temperature carbon – carbon supercapacitor using ionic liquid as electrolyte. *J Power Sources* 2007;165:922–7.
- [10] Abdallah T, Lemordant D, Claude-montigny B. Are room temperature ionic liquids able to improve the safety of commercial supercapacitors organic electrolytes without degrading the performances? *J Power Sources* 2012;201:353–9.
- [11] Environ E. Environmental Science Exploring the large voltage range of carbon/carbon supercapacitors in aqueous lithium sulfate electrolyte, vol. 5; 2012. p. 9611–7.
- [12] Guan BY, Kushima A, Yu L, Li S, Li J, Wen X, et al. Coordination polymers derived general synthesis of multishelled mixed metal-oxide particles for hybrid supercapacitors. *Adv Mater* 2017;29:1–8.
- [13] Rolda S, Barreda D, Granda M, Mene R, Santamarí R, Blanco C. An approach to classification and capacitance expressions in electrochemical capacitors technology. *Phys Chem Chem Phys* 2015;17:1084–92.
- [14] Chandra A. Supercapacitors: an alternate technology for energy storage. *Proc. Natl. Acad. Sci. Sect. A Phys. Sci.* 2012;82:79–90.
- [15] Xiao JQ, Lu Q, Chen JG, Xiao JQ. Nanostructured electrodes for high-performance pseudocapacitors. *Angew Chem Int Ed* 2013;52:1882–9.
- [16] Fan Z, Yan J, Wei T, Zhi L, Ning G, Li T. Asymmetric supercapacitors based on graphene/MnO₂ and activated carbon nanofiber electrodes with high power and energy density. *Adv Funct Mater* 2011;21:2366–75.
- [17] Hwang JY, Li M, El-kady MF, Kaner RB. Next-generation activated carbon Supercapacitors: a simple step in electrode processing leads to remarkable gains in energy density. *Adv Funct Mater* 2017;25:2–9.
- [18] Pang H, Li X, Zhao Q, Xue H, Lai W, Hu Z. Nano Energy One-pot synthesis of heterogeneous Co₃O₄-nanocube/Co(OH)₂-nanosheet hybrids for high-performance flexible asymmetric all-solid-state supercapacitors. *Nanomater Energy* 2017;35:138–45.
- [19] Kong S, Cheng K, Ouyang T, Gao Y, Ye K, Wang G. Facile electrodeposition processed of RuO₂-graphene nanosheets-CNT composites as a binder-free electrode for electrochemical supercapacitors. *Electrochim Acta* 2017;246:433–42.
- [20] Kate RS, Khalate SA, Deokate RJ. Overview of nanostructured metal oxides and pure nickel oxide (NiO) electrodes for supercapacitors: a review. *J Alloy Comp* 2018;734:89–111.
- [21] Salunkhe RR, Kaneti YV, Yamauchi Y. Metal – organic framework-derived nanoporous metal oxides toward supercapacitor applications: progress and prospects. *ACS Nano* 2017;11:5293–308.
- [22] Prasankumar T, Aazem VSI, Raghavan P, Ananth KP, Biradar S, Ilangoan R, et al. Microwave assisted synthesis of 3D network of Mn/Zn bimetallic oxide-high performance electrodes for supercapacitors. *J Alloy Comp* 2017;695:2835–43.
- [23] Paterson-beedle M, Macaskie LE, Lee CH, Hriljac JA. Utilisation of a hydrogen uranyl phosphate-based ion exchanger supported on a biofilm for the removal of cobalt, strontium and caesium from aqueous solutions. *Hydrometallurgy* 2006;83:141–5.
- [24] Jeffrey RDD, Robert CH, Zubieta J. The first organically templated layered cobalt Phosphates: hydrothermal syntheses and crystal structures of [H₃N(CH₂)₃NH₃]_{0.5}[Co(PO₄)]·0.5H₂O and [H₃N(CH₂)₄NH₃]_{0.5}[Co(PO₄)]. *J Solid State Chem* 1996;273:270–3.
- [25] Feng P, Bu X, Stucky GD. Synthesis and characterizations of a polymorphic sodium cobalt phosphate with edge-sharing Co²⁺ octahedral chains. *J Solid State Chem* 1997;131:160–6.
- [26] Hautier G, Jain A, Ong SP, Kang B, Moore C, Doe R, et al. Phosphates as lithium-ion battery cathodes: an evaluation based on high-throughput ab initio calculations. *Chem Mater* 2011;23:3495–508.
- [27] Centi G. Vanadyl pyrophosphate - a critical overview. *Catal Today* 1993;16:5–26.
- [28] Pang H, Yan Z, Wang W, Chen J, Zhang J, Zheng H. Facile fabrication of NH₄CoPO₄·H₂O nano/microstructures and their primarily application as electrochemical supercapacitor. *Nanoscale* 2012;4:5946–53.
- [29] Pang H, Yan Z, Wang W, Wei Y, Li X, Li J. Template-free controlled fabrication of NH₄MnPO₄·H₂O and Mn₂P₂O₇ micro-nanostructures and study of their electrochemical properties. *Int. J. Electrochem. Sci* 2012;7:12340–53.
- [30] Li B, Gu P, Feng Y, Zhang G, Huang K, Xue H. Ultrathin nickel – cobalt phosphate 2D nanosheets for electrochemical energy storage under aqueous/solid-state electrolyte. *Adv Funct Mater* 2017;27:1–11.
- [31] Xi Y, Dong B, Dong Y, Mao N, Ding L, Shi L, et al. Well-defined, nanostructured, amorphous metal phosphate as electrochemical pseudocapacitor materials with high capacitance. *Chem Mater* 2016;28:1355–62.
- [32] Mirghni AA, Momodu D, Oyedotun KO, Dangbegnon JK, Manyala N. Electrochemical analysis of Co₃(PO₄)₂·4H₂O/graphene foam composite for enhanced capacity and long cycle life hybrid asymmetric capacitors. *Electrochim Acta* 2018;283:374–84.
- [33] Mirghni AA, Madito MJ, Oyedotun KO, Masikhwa TM, Ndiaye NM, Ray SJ, et al. A high energy density asymmetric supercapacitor utilizing a nickel phosphate/graphene foam composite as the cathode and carbonized iron cations adsorbed onto polyaniline as the anode. *RSC Adv* 2018;8:11608–21.
- [34] Lee C, Wei X, Kysar JW, Hone J. Measurement of the elastic properties and intrinsic strength of monolayer graphene. *Science* 2008;321:385–8.
- [35] Mirghni AA, Madito MJ, Masikhwa TM, Oyedotun KO, Bello A, Manyala N. Hydrothermal synthesis of manganese phosphate/graphene foam composite for electrochemical supercapacitor applications. *J Colloid Interface Sci* 2017;494:325–37.
- [36] Barzegar F, Bello A, Fashedemi OO, Dangbegnon JK, Momodu DY, Taghizadeh F, et al. Synthesis of 3D porous carbon based on cheap polymers and graphene foam for high-performance electrochemical capacitors. *Electrochim Acta* 2015;180:442–50.
- [37] Bergerhoff G, Berndt M, Brandenburg K. Evaluation of crystallographic data with the program diamond. *J Res Natl Inst Stand Technol* 1996;101:221–5.
- [38] Vlassiok I, Smirnov S, Ivanov I, Fulvio PF, Dai S, Meyer H, et al. Electrical and thermal conductivity of low temperature CVD graphene: the effect of disorder. *Nanotechnology* 2011;22:1–9.
- [39] May P, Lazzeri M, Herziger F, Callens G, Reparaz JS, Hoffmann A, et al. Signature of the two-dimensional phonon dispersion in graphene probed by double-resonant Raman scattering. *J. Phys. Rev.* 2013;75402:1–6.
- [40] Paraguassu W, Freire PTC, Lemos V, Lala SM, Montoro LA, Rosolen JM. Phonon calculation on olivine-like LiMPO₄ (M = Ni, Co, Fe) and Raman scattering of the iron-containing compound. *J Raman Spectrosc* 2005;4:213–20.
- [41] Sahana MB, Vasu S, Sasikala N, Anandan S, Sepelri-amin H, Sudakar C. Raman spectral signature of Mn-rich nanoscale phase segregations in carbon free LiFe_{1-x}Mn_xPO₄ prepared by hydrothermal technique. *RSC Adv* 2014;4:64429–37.

- [42] Casadio F, Bezúr A, Fiedler I, Muir K, Trad T, MacCagnola S. Pablo Picasso to Jasper Johns: a Raman study of cobalt-based synthetic inorganic pigments. *J Raman Spectrosc* 2012;43:1761–71.
- [43] Kim T, Son D, Cho J, Park B. Enhancement of the electrochemical properties of o-LiMnO₂ cathodes at elevated temperature by lithium and fluorine additions. *J Power Sources* 2006;154:268–72.
- [44] Reina A, Jia X, Ho J, Nezich D, Son H, Bulovic V, et al. Large area , few-layer graphene films on arbitrary substrates by chemical vapor deposition. *Nano Lett* 2009;9:30–5.
- [45] Gao Y, Mi L, Wei W, Cui S, Zheng Z, Hou H, et al. Double metal ions synergistic effect in hierarchical multiple sulfide microflowers for enhanced supercapacitor performance. *ACS Appl Mater Interfaces* 2015;7:4311–9.
- [46] You A, Be MAY. In I. Studies of the oxidation states of phosphorus gettered silicon substrates using X- ray photoelectron spectroscopy and transmission electron microscopy. *J Appl Phys* 2013;113:1–7.
- [47] Qiu C, Ai L, Jiang J. Layered phosphate-incorporated nickel – cobalt hydrosilicates for highly Efficient oxygen evolution electrocatalysis. *ACS Sustainable Chem Eng* 2018;6:4492–8.
- [48] Sing KSW. Reporting physisorption data for gas/solid systems with special reference to the determination of surface area and porosity. *Pure Appl Chem* 1982; 54:2201–18.
- [49] Masikhwa TM, Madito MJ, Momodu DY. High performance asymmetric supercapacitor based on CoAl-LDH/GF and activated carbon from expanded graphite. *RSC Adv* 2016;6:46723–32.
- [50] Akinwolemiwa B, Peng C, Chen GZ. Redox electrolytes in supercapacitors. *J Electrochem Soc* 2015;162:A5054–9.
- [51] Fan X, Yu C, Ling Z, Yang J, Qiu J. Hydrothermal synthesis of phosphate-functionalized carbon nanotube-containing carbon composites for supercapacitors with highly stable performance. *ACS Appl Mater Interfaces* 2013;5:2104–10.
- [52] EC-lab software user's manual version 10.38-. August 2014.
- [53] Sluyters-Rehbach M. Impedances of electrochemical Systems : terminology , nomenclature and representation part 1: cells with metal electrodes and liquid solutions. *Pure Appl Chem* 1994;66:1831–91.
- [54] Li H, Wang J, Chu Q, Wang Z, Zhang F, Wang S. Theoretical and experimental specific capacitance of polyaniline in sulfuric acid. *J Power Sources* 2009;190: 578–86.
- [55] Wang B, Liu Q, Qian Z, Zhang X, Wang J, Li Z, et al. Two steps in situ structure fabrication of Ni e Al layered double hydroxide on Ni foam and its electrochemical performance for supercapacitors. *J Power Sources* 2014;246:747–53.
- [56] Oyedotun KO, Madito MJ, Momodu DY, Mirghni AA, Masikhwa TM, Manyala N. Synthesis of ternary NiCo-MnO₂nanocomposite and its application as a novel high energy supercapattery device. *J Chem Eng* 2018;335:416–33.
- [57] Chen X, Cheng M, Chen D, Wang R. Shape-controlled synthesis of Co₂P nanostructures and their application in supercapacitors. *ACS Appl Mater Interfaces* 2016;8:3892–900.
- [58] Ma X-J, Zhang W-B, Kong L-B, Luo Y-C, Kang L. Electrochemical performance in alkaline and neutral electrolytes of a manganese phosphate material possessing a broad potential window. *RSC Adv* 2016;6:40077–85.